

# An Additive Millimeter-Scale Fabrication Method for Soft Biocompatible Actuators and Sensors

Sheila Russo,\* Tommaso Ranzani, Conor J. Walsh, and Robert J. Wood

A hybrid manufacturing paradigm is introduced that combines pop-up book microelectromechanical systems (MEMS) manufacturing with soft-lithographic techniques to produce millimeter-scale mechanisms with embedded sensing and user-defined distributed compliance. This method combines accuracy, flexibility in material selection, scalability, and topological complexity with soft, biocompatible materials and microfluidics, paving the way for applications of soft fluid-powered biomedical robotics. This paper proposes two classes of fully soft fluidic microactuators and two integration strategies to demonstrate the hybrid soft pop-up actuators. Fatigue properties, blocked torque, maximum deflection, stiffness, and maximum speed are analyzed and the performance of the hybrid mechanisms is compared to their fully soft counterparts. The manufacturing approach allows integrating capacitive sensing elements in the mechanisms to achieve proprioceptive actuation. Multiple hybrid soft pop-up actuators are combined into a multi-articulated robotic arm that is integrated with current flexible endoscopes to improve distal dexterity and enable tissue retraction in an *ex vivo* proof of concept experiment.

## 1. Introduction

Minimally invasive surgical procedures are currently performed through long, flexible instruments, such as endoscopes in the gastrointestinal (GI) tract, that allow navigation toward the surgical target through a remote access port, as is done in natural orifice transluminal endoscopic surgery.<sup>[1,2]</sup> However the flexibility required for safe navigation conflicts with the forces and dexterity that can be provided distally, and causes the loss of sensor feedback, limiting current therapeutic capabilities of endoscopes.<sup>[3]</sup> Efforts to improve these therapeutic capabilities, and enable procedures that are currently difficult to perform (such as endoscopic submucosal dissection—ESD),<sup>[4,5]</sup> are limited by the engineering challenges of fabricating distally actuated, safe, miniaturized, smart, and articulated structures. Present solutions mainly rely on cable-driven mechanisms, which have however limitations such as cable friction and backlash that can affect accuracy, controllability, and thus the

intuitiveness of the system.<sup>[6]</sup> Soft robotics represents a promising technology in this field because soft robots are constructed from compliant and flexible materials, resulting in machines that can safely interact with the surrounding environment.<sup>[7,8]</sup> They have already found applications in several research fields including the creation of biomimetic devices (given that the majority of the animal kingdom is mostly or entirely soft),<sup>[9–12]</sup> wearable robots,<sup>[13]</sup> and medical robots.<sup>[14]</sup> However, the low elastic modulus of soft materials can limit the interaction forces between the robots and the surgical target. To resolve the paradox of generating large forces from soft devices, stiffening mechanisms can be exploited,<sup>[15]</sup> such as granular jamming that has been integrated in a soft manipulator in order to effectively apply forces on a desired surgical target.<sup>[16]</sup> Soft biomedical robots are typically centimeter-scale<sup>[17]</sup> or larger but the current

trend in minimally invasive procedures is to perform surgical tasks through small and remote entry points relative to the surgical target,<sup>[18]</sup> thus requiring millimeter-scale systems. Prior examples of soft millimeter-scale mechanisms include flexible microactuators for building robotic manipulators and grippers constructed by casting silicone rubber and nylon fibers in micromolds fabricated using electrical discharge machining,<sup>[19]</sup> soft microtentacles for grasping delicate objects consisting of elastomeric microtubes fabricated with a direct peeling-based soft-lithographic technique,<sup>[20]</sup> and a soft miniature hand fabricated through casting in micromolds and bonding silicone rubber through excimer light irradiation.<sup>[21]</sup> The forces that these actuators can exert are restricted to the millinewton range, thus suggested biomedical applications are limited to low-force surgical tasks, such as those performed in retinal surgery<sup>[22]</sup> and neurosurgery.<sup>[23]</sup> These limitations motivate the need for new millimeter-scale manufacturing technologies that combine soft materials with precision mechanisms to achieve distal articulation, integrated sensing, and effective force transmission with compliant, back-drivable, and safe devices for minimally invasive surgery.

The “pop-up book microelectromechanical systems (MEMS)” manufacturing method creates 3D microstructures based on folding of multilayer rigid-flex laminates,<sup>[24]</sup> and enables fabrication of highly complex structures with embedded actuation and sensing.<sup>[25]</sup> Surgical applications of pop-up mechanisms have been proposed as self-assembling force sensors

Dr. S. Russo, Dr. T. Ranzani, Prof. C. J. Walsh, Prof. R. J. Wood  
Wyss Institute for Biologically Inspired Engineering  
Harvard John A. Paulson School of Engineering and Applied Sciences  
60 Oxford Street, Cambridge, MA 02138, USA  
E-mail: sheilarusso85@gmail.com, srusso@seas.harvard.edu

 The ORCID identification number(s) for the author(s) of this article can be found under <https://doi.org/10.1002/admt.201700135>.

DOI: 10.1002/admt.201700135

for catheters,<sup>[26]</sup> and mechanisms for deflecting electrosurgical tools in endoscopic procedures.<sup>[27]</sup>

In this paper, we leverage our previous work, where we introduced a first proof of concept of combining the pop-up book MEMS fabrication technology with techniques from soft lithography, to demonstrate a hybrid manufacturing paradigm, called “soft pop-up.”<sup>[28]</sup> Here, we present for the first time, a method for monolithic integration of soft materials and soft fluidic microactuators with other mechanical and sensing components, without the need for manual intervention to assemble discrete parts (thus guaranteeing a more accurate and faster fabrication process). We have also expanded the materials portfolio to exclusively biocompatible materials thus paving the way to develop smaller, smarter, softer robots for medical/surgical applications. We present and analyze the fabrication process in depth, assessing its reliability with chemical surface characterizations and mechanical peel strength tests. Our method combines the accuracy, flexibility in material selection, scalability, and topological complexity of pop-up book MEMS with soft, biocompatible materials and microfluidics from the realm of soft lithography. This hybrid concept also enables soft fluidic actuation to safely interact with biological tissue without the need for high voltages or temperatures found in other small-scale actuators (e.g., piezoelectric bimorph actuators which require up to 200 V<sup>[29]</sup>). In addition, we extensively characterize and compare the performance of two classes of hybrid soft pop-up actuators and their fully soft counterparts to investigate, for the first time, the benefits of integrating rigid components and rigid mechanisms with soft materials and soft fluidic microactuators. In particular, we focus on life cycles, blocked force and torque, deflection, stiffness, and speed. This ultimately led to a comparison of different performance indices between the hybrid and the fully soft actuators, such as work and power output, and power density. Furthermore, we thoroughly characterize and model proprioceptive actuators with embedded capacitive

sensing at different dimensions, demonstrating scalability of the process. Finally, we demonstrate for the first time an ex vivo experiment of a soft pop-up multiarticulated robotic arm, fabricated entirely with biocompatible materials and integrated on a flexible endoscope to evaluate the possibility of performing tissue countertraction (necessary for the resection of neoplasms in the gastrointestinal tract).

## 2. Results

Two different sets of soft fluidic microactuators (SFMA) and two different designs of soft pop-up actuators are proposed (Figure 1). The two SFMA consist of an axial fully soft actuator (AFS) and a bending fully soft actuator (BFS). The AFS is a circular cross-section chamber that expands into a hemispherical balloon upon pressurization with water (see Figure 1A). The BFS has a rectangular chamber that allows bending based on layer and material asymmetry (see Figure 1E). Biocompatible silicone elastomers have been selected for fabrication of the SFMA. The AFS and BFS actuators are also integrated in a pop-up structure exploiting our hybrid manufacturing approach to build soft pop-up actuators: the AFS is fully embedded (thus we will refer to this mechanism as internal microballoon joint—IMJ) in a mechanism that converts axial deformation into a rotational degree of freedom (DOF) (Figure 1B,C), whereas the BFS is bonded externally (thus we will call it external microballoon joint—EMJ) with respect to the pop-up structure (Figure 1F,G). These soft pop-up mechanisms (IMJ and EMJ) are created from fiber-reinforced epoxy sheets (254  $\mu\text{m}$  thick) as the structural material and polyimide film (25  $\mu\text{m}$ ) as a flexible material. Gaps in the structural material expose the embedded flexible material, creating folding flexure joints that define the articulation in IMJ and EMJ actuators. These layers are bonded with 3M 9877 pressure-sensitive adhesive (Figure 1D,H).

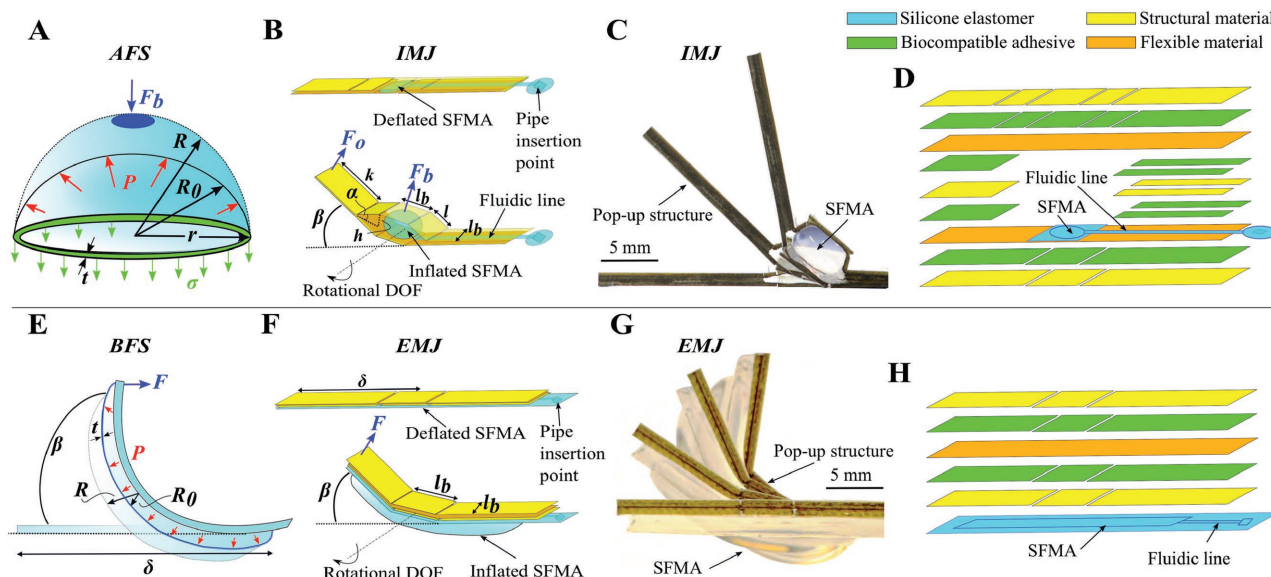


**Figure 1.** Fully soft and soft pop-up mechanisms. A,E) AFS during expansion, modeled using Laplace's law for a thin-walled sphere and BFS during inflation, modeled using Laplace's law for a thin-walled cylindrical vessel. B,F) IMJ and EMJ in deflated and inflated states with model parameters. C,G) IMJ and EMJ prototype during bending upon pressurization with water. D,H) IMJ and EMJ exploded view showing all layers.

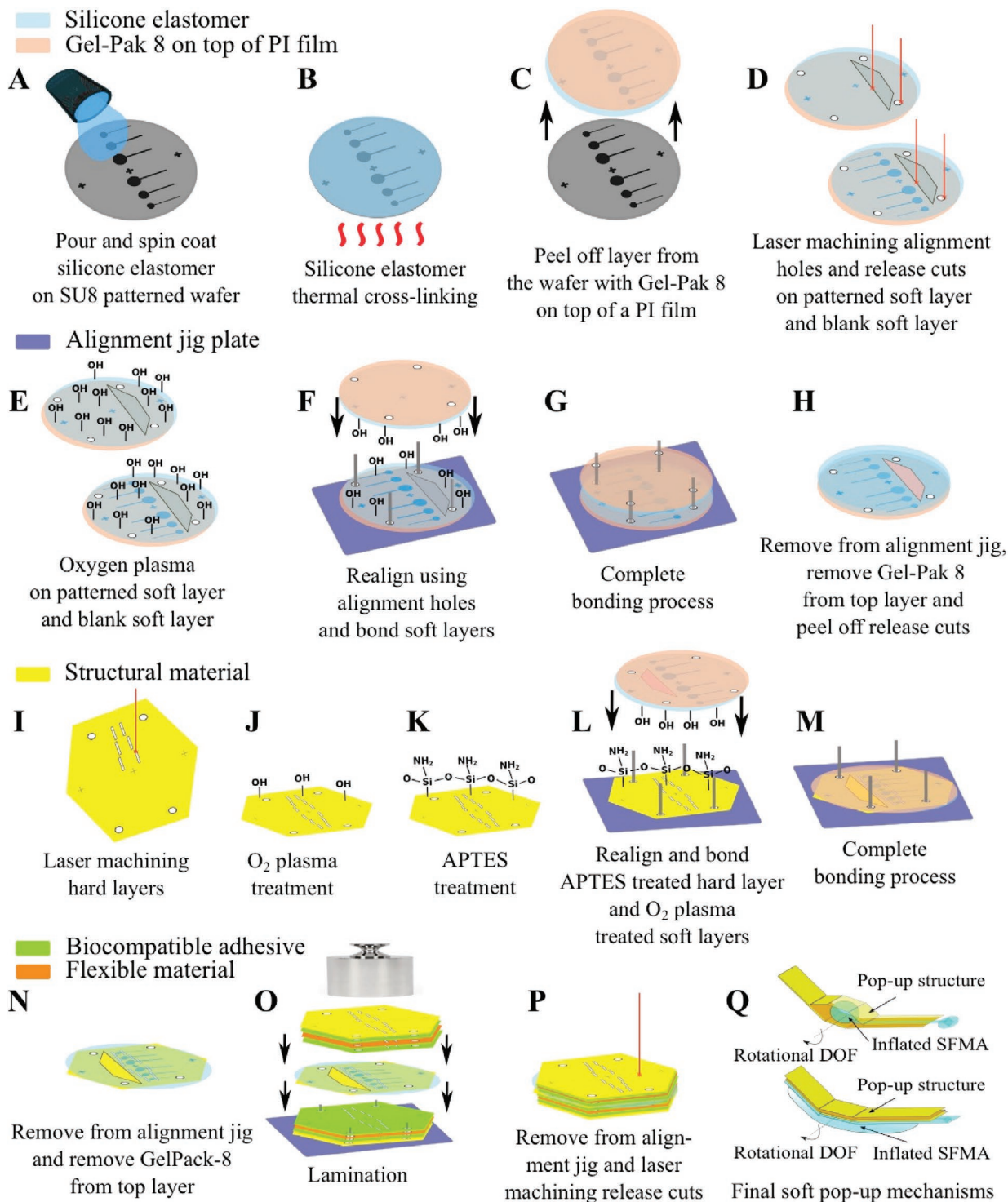


**Figure 2.** Overview of the soft pop-up manufacturing method. SFMA are manufactured using A) soft lithography, B) soft layers are cured, C) peeled off from the wafer mold, D) laser machined, E) O<sub>2</sub> plasma treated, and F) realigned G,H) to be bonded. Hard layers are I) laser machined, J) chemically modified with O<sub>2</sub> plasma and K) APTES, L) realigned, and M) bonded to the soft layers. N) The resulting hard/soft layer is O) laminated and P) a final laser machining step releases Q) the mechanisms from the surrounding substrate.

Integration of soft components in pop-up book MEMS is achieved by first fabricating the SFMA with soft lithography and laser machining (Figure 2A–H). The actuators are integrated into laminated pop-up structures by chemically modifying

the polymer surfaces to achieve an irreversible chemical bond between the soft and the hard layers (combining oxygen plasma and amino-silane coupling agent (3-Aminopropyl)triethoxysilane (APTES)), as shown in Figure 2I–M. In our previous

work,<sup>[28]</sup> SFMA were cut and positioned manually with respect to the hard layers, thus affecting precision and repeatability of the process: assembly was performed manually by realigning the actuators visually under a microscope, and had to be done quickly in order to guarantee a successful chemical bond. In the present work, we have developed a technique to obviate the need for manual cutting and assembling of soft components, thus guaranteeing a more accurate and faster fabrication of the actuators. Soft layers are transferred on a flexible support and aligned with the laser coordinate system by means of fiducial markers that are embossed on the silicon wafer mold (Figure 2C,D). During laser machining, holes are created on the soft layer and the flexible support to allow realignment and bonding/integration with the rest of the laminate by using precision dowel pins (Figure 2F,L). After the layers are laminated, a final laser machining step releases the soft pop-up mechanisms from the surrounding substrate (Figure 2N–Q).

We demonstrate the scalability of this hybrid approach by fabricating IMJ and EMJ prototypes at three different scales: 5,

2.5, and 1.25 mm (which correspond to the width of the actuator  $l_b$ , indicated in Figure 1B,F). These dimensions were chosen to achieve mechanisms that can be mounted either externally with respect to operative gastrointestinal endoscopes (typical outer diameter 11.1–15 mm) or passed through the endoscope working channel (2.8–4.2 mm).<sup>[30]</sup> Accordingly, AFS and BFS actuators were fabricated at the same scales: the radius  $r$  of the AFS is 1.5, 0.65, and 0.375 mm (respectively, for the 5, 2.5, and 1.25 mm scales) and the length and width of the BFS chambers are  $19 \times 1$ ,  $10.45 \times 1$ , and  $10 \times 0.5$  mm (respectively, for the 5, 2.5, and 1.25 mm scales). Photos of the fabrication workflow for the soft pop-up actuators are shown in **Figure 3**. For the IMJ, the chemical bonding phase between hard layer surfaces and the SFMA is shown in Figure 3A. SFMA and fluidic line integration in the IMJ laminate, before and after release cuts, is shown in Figure 3B,C, respectively. A side view of the IMJ laminate is illustrated in Figure 3D. Similarly, SFMA integration in the EMJ laminate is shown in Figure 3E and a side view of the EMJ laminate is presented in Figure 3F. Release

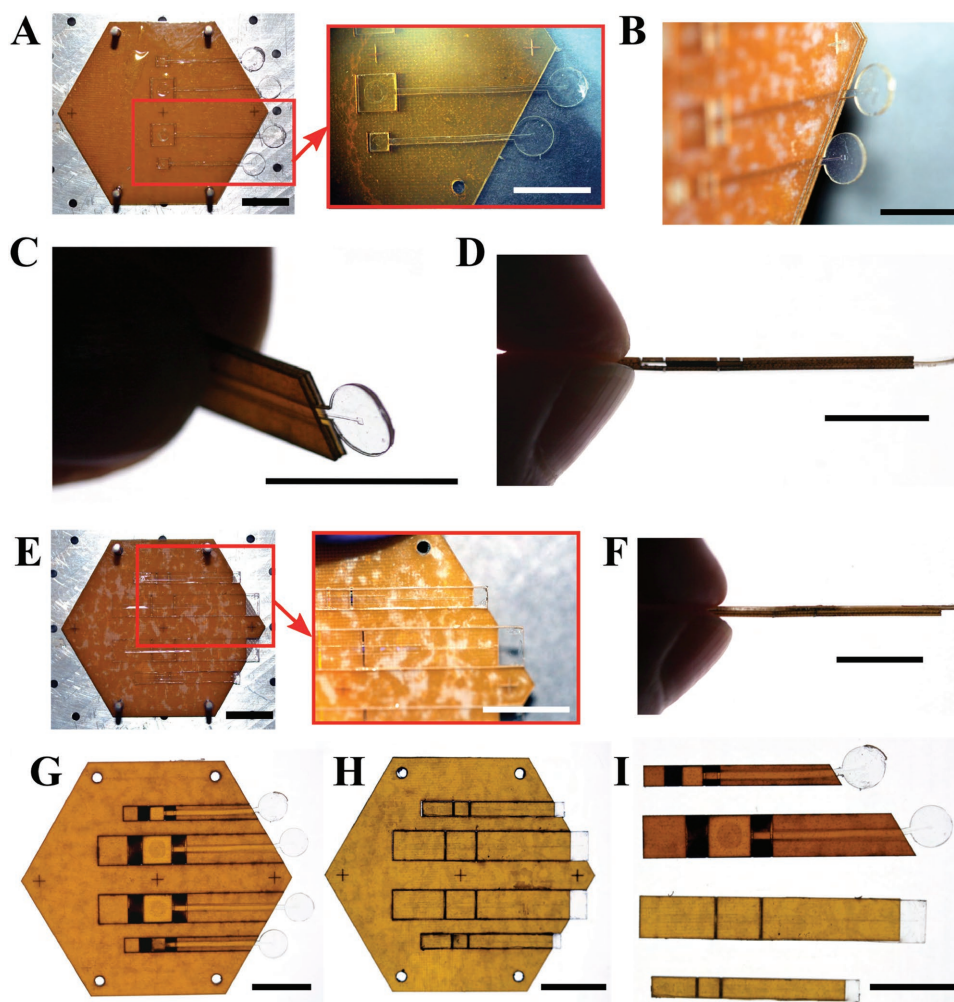


**Figure 3.** Fabrication process of the soft pop-up actuators. Scale bar in all images is 10 mm. A) SFMA are chemically bonded on the IMJ sublimate (layers are aligned using precision dowel pins), with detail of the integrated actuators. B) IMJ laminate with detail of integrated fluidic lines. C) Detail of a fluidic line integrated inside the IMJ laminate after release cuts. D) IMJ laminate profile. E) Aligned and bonded SFMA on the EMJ laminate, and detail of the integrated actuators. F) EMJ laminate profile. G,H) Release cuts on the IMJ and EMJ to release the mechanisms from the laminate scaffold. I) Final prototypes of IMJ (top) and EMJ (bottom).

cuts to remove the mechanisms from the laminate scaffold are shown in Figure 3G,H, and the final prototypes are presented in Figure 3I.

### 2.1. Biocompatible Silicone Elastomers

Soft robotic fluidic actuators are often made of silicone elastomers (e.g., Ecoflex or Dragon Skin, Smooth-On, Inc., USA) and typically rely on 3D printed molds. For millimeter-scale actuators, 3D printing is inappropriate and instead we turn to techniques from soft lithography-based microfluidics including the creation of lithographic micromolds and plasma bonding. In our previous work,<sup>[28]</sup> we demonstrated the possibility of mixing Sylgard 184 together with Dragon Skin at different ratios to allow oxygen plasma bonding between soft layers and to tune the mechanical properties of the polymeric mixture (thus increasing the strength to failure and decreasing the stiffness) in order to fabricate soft fluidic microactuators through soft lithography. The main issue with this approach is that Dragon Skin does not meet the requirement of biocompatibility that is necessary to develop mechanisms for medical/surgical applications.

In this paper, SFMA are manufactured using biocompatible<sup>[31,32]</sup> silicone elastomers (NuSil Technology, CA, USA). Silicone elastomers with different shore hardnesses have been selected: MED4-4220 (17A durometer), MED-4011 (27A durometer), MED-4044 (40A durometer), and MED-6033 (50A durometer). Stress–strain tests (according to standard ISO 37:2005(E)) of these four different materials are reported in Figure S1 (Supporting Information) together with stress–strain of Sylgard 184 as a reference. These silicone elastomers are more stretchable and have a higher tear strength than Sylgard 184 (which is usually used in soft lithography), which makes them better candidates for fabricating soft actuators that can exhibit large deformations at relatively low pressures.

### 2.2. Biocompatible Adhesive

Given their similarity to printed circuit boards, pop-up mechanisms are usually fabricated using DuPont Pyralux FR0100 acrylic adhesive<sup>[24]</sup>—a thermoset film adhesive engineered for laminated composites. Here, we select a biocompatible<sup>[33]</sup> medical adhesive (3M 9877) to avoid risks related to cytotoxicity. In addition, 3M 9877 is an instantaneous pressure sensitive adhesive, obviating the need for heat to cure and speeding up the fabrication process by eliminating  $\approx 5$  h, with respect to our previous work.<sup>[28]</sup> The adhesive peel strength was tested (according to standard ASTM D903-98(2010)) on different substrates including fiber-reinforced epoxy (FR4), copper (Cu), polyimide (PI), and stainless steel (SS). Peel strength results of 3M 9877 are reported in Table S1 (Supporting Information) along with the peel strength of DuPont Pyralux FR0100 as a reference.

### 2.3. Chemical Bond Characterization

In order to verify the success of chemical functionalization with APTES, the surfaces of unmodified and modified substrates

were assessed by water contact angle measurements. Water contact angles were measured on the surfaces of pristine, O<sub>2</sub> plasma treated, and amine-functionalized (APTES) SS, FR4, Cu, and PI using a sessile drop technique (Attention Theta Lite). Each experiment was repeated at least five times and results are reported in Table S2 (Supporting Information). After O<sub>2</sub> plasma treatment, water contact angles decreased regardless of the substrate type with respect to the pristine substrate. After the APTES treatment, hydrophobicity increased for all materials and water contact angle values are between the values of pristine and O<sub>2</sub> plasma treated substrates, suggesting that the surfaces are modified with the silane.

In addition to characterizing surface properties, we verified the success of the chemical bond between soft and hard material layers. The strength of the chemical bond, formed between the APTES-treated rigid substrates and the O<sub>2</sub> plasma-treated silicone elastomers, is determined with peel strength tests (ASTM D903-98(2010)). Samples were prepared by bonding MED4-4220 and MED-6033 on top of different substrates: SS, FR4, Cu, and PI. Results are reported in Table S3 (Supporting Information). For each test, the silicone elastomer failed without delaminating from the substrate.

### 2.4. Fatigue Testing

We assessed fatigue of the AFS and BFS actuators by measuring pressure–volume (*PV*) hysteresis curves before starting the test and after 20, 50, 100, 200, and 500 cycles (Figure S2, Supporting Information). For each cycle, the actuators were inflated with water until full deformation (which has been determined during deflection testing, discussed below) and then deflated until the pressure returned to zero using a syringe pump (Harvard Apparatus, Pump 11 Elite, USA) and a pressure sensor (BSP B010-EV002-A00A0B-S4, Balluff, USA). We stopped at 500 cycles as this would translate to 8.3 cycles per minute during a surgical operation of 60 min. The number of cycles per minute that the IMJ and EMJ are able to achieve is constrained by their maximum speed (which has been determined during maximum speed testing). Two different scales (5 and 1.25 mm) were tested for each actuator since the thickness, *t* (as defined in Figure 1A,E), of the silicone membrane is the maximum and minimum in the prototypes: 0.3 and 0.15 mm, respectively. None of the actuators failed, but *PV* curves show that lower pressures and greater volumes are required to achieve the same deformation regardless of the type and scale of the actuator, likely due to relaxation of the polymer chains. For this reason, pressure control would be preferable in a real application scenario. Table S4 (Supporting Information) shows the reduction of pressure during cyclic testing in percentage with respect to the pressure needed to inflate the actuator during the first cycle.

### 2.5. Blocked Force and Torque Testing

We evaluated blocked force for the AFS and blocked torque for the BFS, IMJ, and EMJ at each scale. Results are shown in Figure 4A–C. Each test was repeated at least three times. Input pressure was measured with a pressure sensor (BSP

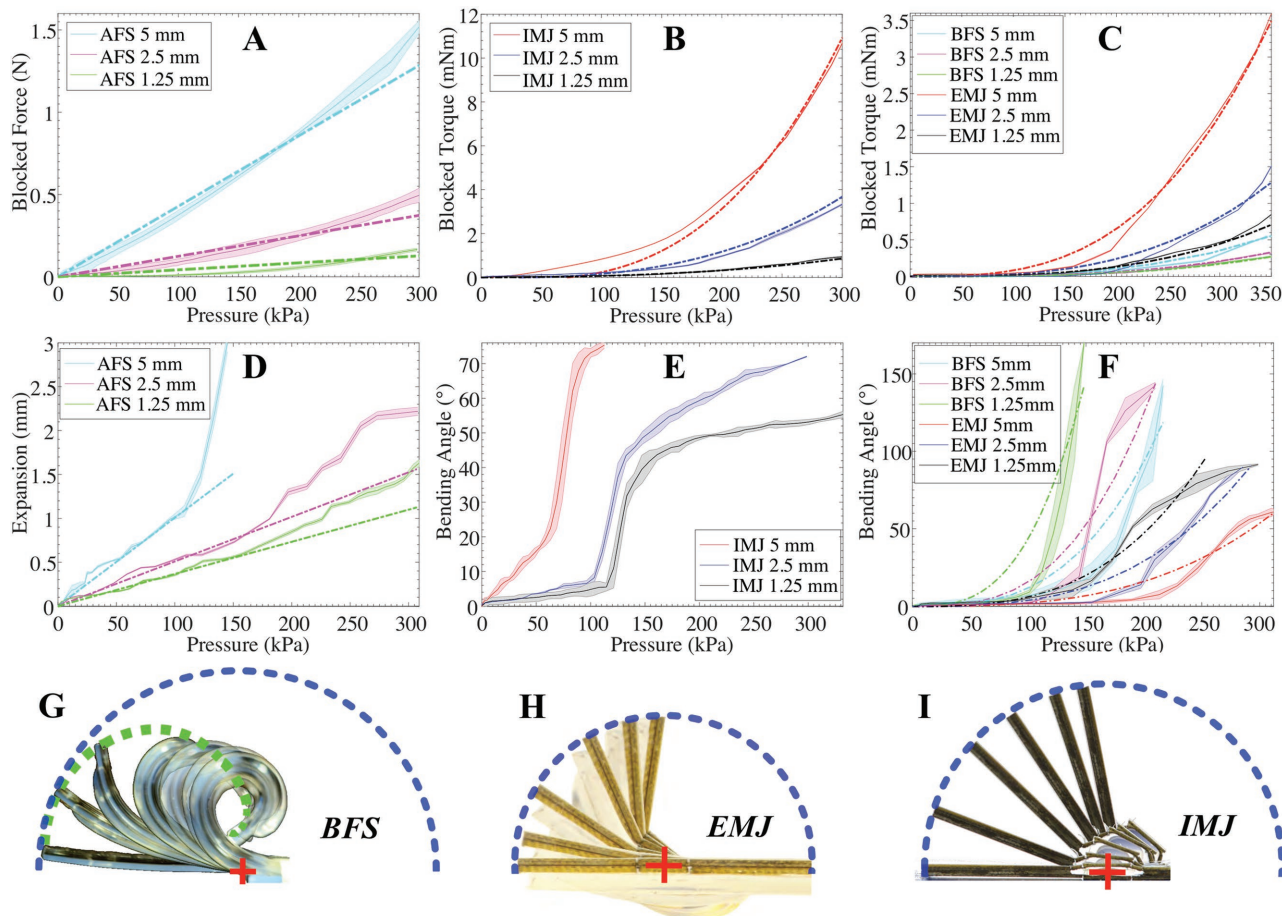


**Figure 4.** Blocked force, blocked torque, and deflection tests. Blocked force test for A) the AFS, B) blocked torque test for the IMJ, and C) the BFS and EMJ. Deflection test for D) the AFS, E) IMJ, F) BFS, and EMJ actuators. All plots (A–F) report data for the actuators at different scales (5, 2.5, and 1.25 mm), the dashed line is the output from the model, the solid line is the mean resulting from three experiments, and the shaded area is the standard deviation. The trajectories captured with a camera respectively of G) the BFS, H) EMJ, and I) IMJ during actuation. The desired trajectory is shown in blue whereas the real trajectory is shown in green.

B010-EV002-A00A0B-S4, Balluff, USA). During each test for the BFS, IMJ, and EMJ, one side of the actuator was fixed with a frame and the other was constrained under a force/torque ( $F/T$ ) sensor (Nano17 Titanium, ATI Industrial Automation, NC, USA) in a straight configuration ( $0^\circ$  bending) at a known distance. A scheme showing the experimental setup is reported in Figure S3 (Supporting Information). AFS actuators were directly put under the  $F/T$  sensor. Since the AFS is fully constrained during the test, we can simply model it by using  $F_b = \pi \Delta P \times r^2$ , where  $F_b$  is the blocked force exerted by the balloon,  $\Delta P$  is the internal pressure, and  $r$  is the radius of the AFS circumference. On the other hand, the IMJ motion is constrained, but the pressurization of the AFS embedded inside the hybrid actuator can still lead to a small deformation ( $\Delta R$ ) of the balloon (due to the flexibility of the polyimide flexures), which was optically measured during the test. In this case, we modeled the AFS using Laplace's law for a thin walled sphere (Figure 1A), and by balancing internal pressure  $\Delta P$  and tension  $\sigma$  at the wall with the force exerted by the balloon  $F_b$ , we can derive the following expression for the force, assuming that the actuator is made of a linear elastic material

$$F_b = \pi \Delta P \Delta R^2 - 2\pi r t E \frac{\Delta R}{R_0} \quad (1)$$

where  $t$  is the thickness of the membrane,  $E$  is the elastic modulus of the silicone elastomer, and  $R$  is the expansion in the axial direction. The output force  $F_o$  of the IMJ can be simply derived from Equation (1) with geometrical considerations of the hybrid actuator design

$$F_o = F_b \left( \frac{l}{l+k} \right) \cos \alpha \quad (2)$$

where  $F_o$ ,  $\alpha$ ,  $k$ , and  $l$  are shown in Figure 1B. The output torque results in  $M_o = F_o \times (k + l + l_b/2)$ .

The maximum blocked force for the AFS actuators is 1.54, 0.49, and 0.17 N, respectively, for the 5, 2.5, and 1.25 mm scales (Figure 4A). The maximum blocked torque for the IMJ is 10.68, 3.34, and 0.94 mN m, respectively, for each scale (Figure 4B). The corresponding forces (dividing these torque values by the moment arm) are: 1.42, 0.51, and 0.17 N, for each scale. This suggests that the force is transmitted efficiently from the

embedded fully soft actuator (AFS) to the soft pop-up mechanism (IMJ). The model is able to predict the experimental data quite accurately.

To model the force  $F$  exerted by the actuators, we also modeled the BFS and EMJ using Laplace's law for a thin walled cylindrical vessel (assuming linear elasticity of the material)

$$P = \frac{Et}{2R_0} \left(1 - \frac{R_0}{R}\right) \quad (3)$$

$$F = \frac{2\pi r}{\delta} \Delta P \Delta R^2 \quad (4)$$

where  $\delta$  is the distance shown in Figure 1E,F. In this case, the output torque is simply  $M = F \times \delta$ . The maximum blocked torque for the BFS actuators is 0.55, 0.32, and 0.27 mN m, respectively, for the 5, 2.5, and 1.25 mm scales; the maximum blocked torque for the EMJ actuators is 3.6, 1.46, and 0.8 mN m, respectively, for the 5, 2.5, and 1.25 mm scales (Figure 4C). Also in this case, the model can quite accurately predict the experimental data. The maximum block torque is 6 $\times$ , 4 $\times$ , and 3 $\times$  greater, respectively, for each scale, when we add the pop-up structure to the actuator. This benefit is mainly related to the hybrid design of the soft pop-up actuator that provides an increase in the stiffness (20–25 $\times$  greater) with respect to the BFS (discussed in Section 2.7).

## 2.6. Deflection Testing

We evaluated the maximum deflections that the AFS, BFS, IMJ, and EMJ actuators are able to achieve by tracking their trajectories using images taken from a camera during unloaded pressurization. Each test was repeated at least three times. During each test, one side of the BFS, IMJ, and EMJ actuators was constrained and the other was left free to move. For the AFS, the base of the actuator was fixed on a flat surface. We modeled the AFS expansion  $h$  (Figure 1A) using the membrane theory for a circular plate

$$h = \frac{\Delta P r^4}{128 \left( \frac{Et^3}{12(1-\nu^2)} \right)} \quad (5)$$

where  $\nu$  is the Poisson's ratio of the silicone elastomer. For the BFS and EMJ actuators, we modeled the actuator as a single flexure and applied beam theory to derive the bending angle  $\beta$  (Figure 1E,F)

$$\beta = 2\pi r \frac{\Delta P \Delta R^2}{EI} \quad (6)$$

where  $E$  is the elastic modulus of the polyimide flexures and the silicone elastomer for the EMJ and BFS actuators, respectively. Results are reported in Figure 4D–F. With regards the AFS (Figure 4D), the analytical model is able to predict the experimental results up to  $\approx$ 100–150 kPa. The actuators deviate from the model at higher pressures.

Generally for the AFS, the larger the scale, the lower the pressure required to expand the actuator. For simplicity, we assumed that the elastic modulus of the MED4-4220 silicone elastomer remains constant during deformation (although this is not strictly true, as shown in Figure S1, Supporting Information). For the IMJ, the balloon requires a minimum pressure to apply the necessary force to the pop-up structure to initiate motion, as shown in the initial portion of Figure 4E. After this initial step, bending is achieved with a small pressure increase. Finally, the actuator saturates because it is constrained mechanically by the pop-up structure. Such behavior is more challenging to model, thus we investigated the possibility of integrating sensing capabilities in the IMJ, to achieve proprioceptive actuation (discussed in Section 2.8). The maximum bending angles for the IMJ are 75.3 $^\circ$ , 72 $^\circ$ , and 55.3 $^\circ$  for the 5, 2.5, and 1.25 mm scale, respectively.

In contrast to the AFS, the BFS requires an initial minimum pressure before the bending can start (regardless of the scale), which is  $\approx$ 100 kPa (Figure 4F). This is likely related to the different change in hydraulic resistance between the actuators' channels and the actuators' chambers among the BFS and AFS. The hydraulic resistance  $R_h$  for a rectangular cross-section is proportional to the ratio between the length  $L$  and the width  $w$  and the height  $h$  of the actuator ( $R_h \propto L/wh^3$  valid when  $h < w$ ). Considering that the height of the channel is the same for all the actuators, the change in hydraulic resistance is determined from the ratio  $L/w$ . In the case of the AFS, the hydraulic resistance of the actuator chamber is approximately one order of magnitude smaller than the resistance of the actuator channel. However, for the BFS the hydraulic resistance of the actuator chamber is approximately half of the resistance of the actuator channel, thus requiring a higher pressure to initiate the deformation. After reaching this pressure, a small pressure increase is necessary to achieve full bending: the actuators bend up to almost 180 $^\circ$  (the free end of the actuator reaches its fixed end, creating a full circle). In this case, the larger the scale, the higher the pressure required to fully bend the actuator. The EMJ exhibits a similar behavior as the BFS. The initial pressure required to start bending is a slightly larger in this case and the maximum bending angle is smaller since it is constrained by the design of the surrounding pop-up structure (Figure 4F). The maximum bending angles are 60.9 $^\circ$ , 89.8 $^\circ$ , and 91.5 $^\circ$  for the 5, 2.5, and 1.25 mm scales, respectively.

One of the primary benefits of the soft pop-up approach is highlighted in Figure 4G–I, where we compare the trajectories of the fully soft bending actuators with the hybrid soft pop-up counterparts. The observed trajectory of the soft pop-up actuators (Figure 4H,I) is a regular circumference arc, centered with a red cross in the center of the hybrid actuators. Whereas the bending fully soft actuator tends to roll around itself (green trajectory in Figure 4G) due to the compliance of the system, deviating from the regular circumference arc (blue trajectory in Figure 4G). Indeed, the rigid structure naturally constraints the actuators to follow a well-defined and regular trajectory, thus defining the kinematics of the actuators.

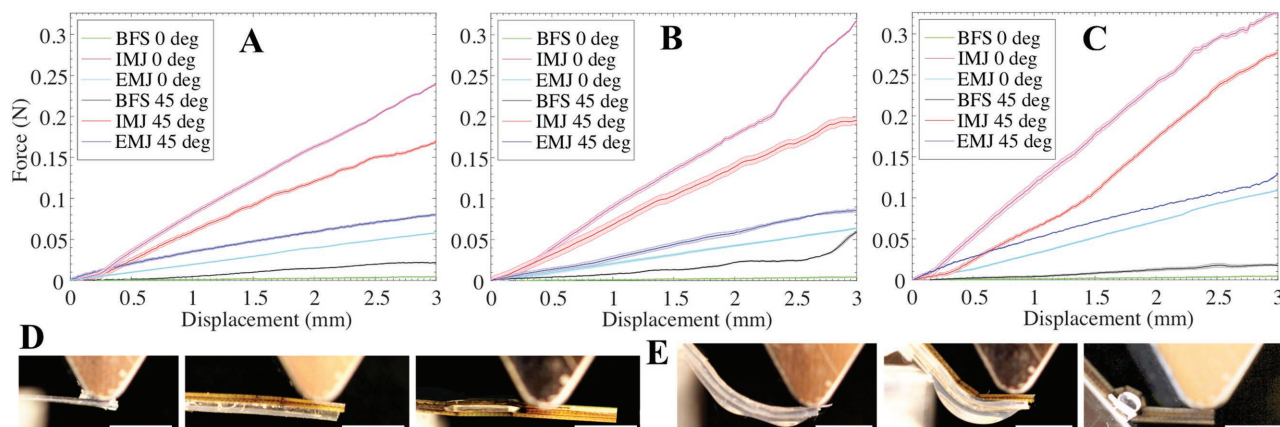


**Figure 5.** Stiffness tests. Bending stiffness results for the BFS, EMJ, and IMJ in rest 0° and actuated 45° conditions at A) 5 mm, B) 2.5 mm, and C) 1.25 mm scale. The solid line is the mean from three experiments and the shaded area is the standard deviation. From the left: BFS, EMJ, and IMJ stiffness test setup at rest, D) 0° condition, and E) actuated (45°) condition. Pressures to achieve the 45° actuated condition for each actuator is reported in Figure 4E,F. Each actuator is fully constrained on the left side and a displacement of 3 mm is imposed on the right side while recording the force. Scale bar in all images is 5 mm.

## 2.7. Stiffness Testing

The bending stiffness of the IMJ and EMJ was characterized and compared to the stiffness of the BFS to assess the effect of the rigid pop-up structure. Bending stiffness values were measured by positioning each actuator with the base fully constrained and imposing a displacement of 3 mm using an Instron materials testing machine while recording the force. Results are reported in Figure 5A–C, respectively for the 5, 2.5, and 1.25 mm scales. The computed stiffness values are summarized in Table S5 (Supporting Information). The test was conducted both in a nonactuated configuration (Figure 5D) and when the actuators were 45° bent (Figure 5E). Each test was repeated three times. The IMJ structure provides with the greatest stiffness, more than 100× that of the BFS, independent of scale. In this case the stiffness is dominated by the polyimide hinges above and below the SFMA (see Figure 1D). Since the thickness of the IMJ remains constant at the different scales, the increase in stiffness is even larger at smaller scales due to the reduced width to height ratio in the structure. In the bent configuration the compliance of the inflated balloon reduces the stiffness by ≈30% (Table S5, Supporting Information). The EMJ provides a significant increase in the stiffness (20–25× greater) with respect to the BFS, which correlates to an increase in the blocked torque, as discussed above. Stiffness values are larger at smaller scales for the same reason as for the IMJ. The stiffness increase is primarily due to the polyimide hinges in parallel with the BFS bonded on top of it (see Figure 1H). In this case, pressurization of the soft actuator leads to an increase in the stiffness of the structure; in the 45° bent configuration the stiffness increase with respect to the nonactuated BFS is ≈30×. The stiffness of the BFS is mainly influenced by the material properties of the silicone elastomers used. In addition, similarly to the EMJ, in the 45° bent configuration the pressurization of the actuator leads to a substantial increase in stiffness.

## 2.8. Proprioceptive Actuation

IMJ actuators at 5, 2.5, and 1.25 mm scales were fabricated with embedded conductive traces along the actuator sides and conductive plates at the top and bottom of the soft balloon (Figure 6A). A secondary conductive trace runs along the primary trace to shield from possible interference due to capacitance coupling. In this way, when the internal balloon inflates, a composite dielectric (consisting of the parallel of water and air connected in series with the elastomer) is formed (Figure 6B) between the two conductive plates. Here, we model the equivalent capacitance as

$$C_{\text{eq}} = \left[ \frac{d_{\text{exp}}}{\epsilon_0 (\pi R^2 (\epsilon_w - \epsilon_a) + \epsilon_a A)} + \frac{d_0}{\epsilon_0 \epsilon_c A} \right]^{-1} \quad (7)$$

where  $\epsilon_0$  is the vacuum permittivity,  $d_{\text{exp}}$  is the distance between the conductive plates,  $R$  is the radius of the balloon,  $\epsilon_w$  is the relative permittivity of water,  $\epsilon_a$  is the relative permittivity of air,  $A$  is the area of the conductive plates,  $\epsilon_c$  is the relative permittivity of the elastomer, and  $d_0$  is the thickness of the SFMA. Capacitance variation is measured with an AD7746 evaluation board (Analog Devices, MA, USA) and bending motion is tracked using photos taken during inflation. Results are reported in Figure 6C. The capacitance is normalized in order to compare different prototypes. There is a slight variation between the experimental results and the model, which can be explained sufficiently by the fact that the model is neglecting the area where there is additional air, shown in yellow of Figure 6B. The actuators used for the experimental results of Figure 6 are IMJ actuators with embedded capacitive sensing. The integration of sensing capabilities (conductive plates and traces) does not affect their mechanical functionality. The relationship between bending angle and pressure for these actuators is shown in Figure 4E. The conductive components of this

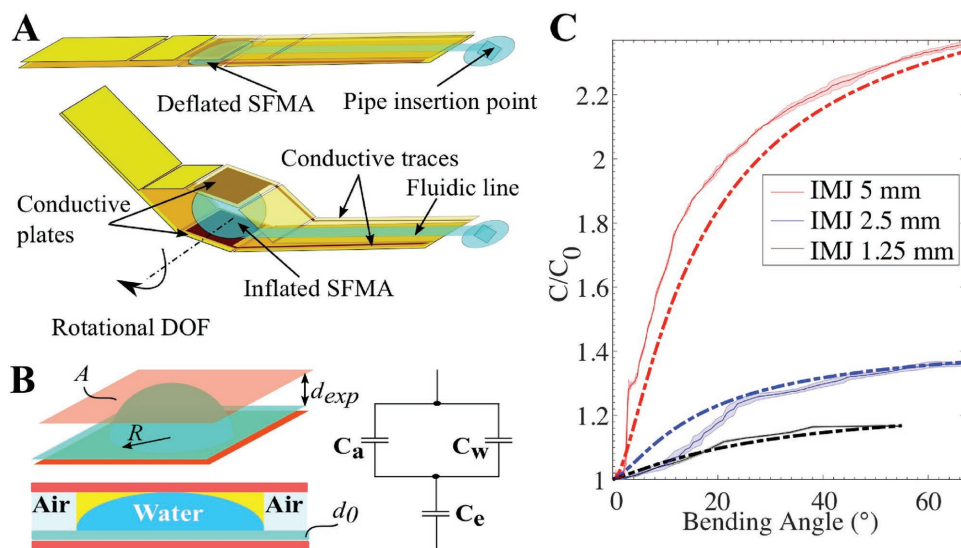


**Figure 6.** Characterization and modeling of proprioceptive actuation. A) Scheme of the integration of conductive traces and conductive plates in the IMJ to achieve proprioceptive actuation. B) Model of the capacitive sensor. C) Characterization of the proprioceptive IMJ actuators at different scales: 5, 2.5, and 1.25 mm. The dashed line is the model, the solid line is the mean resulting from three experiments, and the shaded area is the standard deviation.

system are realized with copper, which can raise some concerns in terms of biocompatibility, but this material could be easily substituted with gold (e.g., deposited by physical vapor deposition). Gold has also been proven to be compatible with the chemical bonding realized through amino-silane (APTES).<sup>[34]</sup>

### 2.9. Maximum Speed

We assessed the maximum speed of each type of actuator at different scales. This test determines the upper limit for each actuator velocity and thus the applicability for various surgical tasks. This test is performed by inflating each actuator until it is fully bent/expanded at the maximum speed of the syringe pump ( $1.47 \text{ mL s}^{-1}$ ). The maximum speed of each actuator is computed by analyzing the associated movies: Movie S1 (Supporting Information) for the AFS and BFS, and Movie S2 (Supporting Information) for the IMJ and EMJ. For the AFS, the expansion happens at a maximum speed of 1.7, 2.6, and  $2.8 \text{ mm s}^{-1}$  for the 5, 2.5, and 1.25 mm scales, respectively. This translates to a maximum bending speed for the different scales of the IMJ actuators of 8.3, 12.6, and  $16.9^\circ \text{ s}^{-1}$ . The BFS actuators have a maximum bending speed of 15, 22.5, and  $120^\circ \text{ s}^{-1}$  for the 5, 2.5, and 1.25 mm scales, respectively. This translates to a maximum bending speed for the different scales of the EMJ actuators of 8.7, 10, and  $18^\circ \text{ s}^{-1}$ . The 1.25 mm scale BFS actuator can bend significantly faster than the other scales mainly because the actuator dimensions and membrane thickness are smaller. The pop-up structure introduces a reduction in the maximum speed that the EMJ can achieve with respect to the BFS, which is almost half for the 5 and 2.5 mm scales and six times smaller for the 1.25 mm scale. This difference is due to the fact that the pop-up structure introduces a higher stiffness (which is even higher at smaller scales, see Table S5,

Supporting Information) and that the soft balloon has to counteract an increased inertia. However, the maximum bending speed for the soft pop-up actuators are in a range from  $8.3$  to  $18^\circ \text{ s}^{-1}$ , which is suitable for medical/surgical applications.

### 2.10. Multiarticulated Soft Pop-Up Robotic Arm

We believe that mechanisms designed and fabricated following the hybrid soft pop-up manufacturing paradigm have potential in augmenting the therapeutic capabilities of current flexible endoscopic instruments. Small-scale, distally actuated mechanisms can enable endoluminal manipulation tasks in endoscopic surgery, e.g., providing the necessary countertraction for safe en bloc resection of neoplasms in the gastrointestinal tract. As a demonstration of these potential benefits, we fabricated a multiarticulated soft pop-up robotic arm (Figure 7) and integrated it onto the tip of an Olympus CF-100L flexible endoscope (13.3 mm in outer diameter). The addition of the arm laminate increases the endoscope diameter by only 1.8 mm. The arm has three DOF and it is composed of (1) a four-bar linkage mechanism, expanded by an AFS, to move the arm with respect to the endoscope vision system (surgical triangulation); (2) a yaw DOF (based on the EMJ actuator); and (3) a pitch DOF (based on the IMJ actuator) to steer an end-effector and perform tissue manipulation (Figure 7A).

In our previous work,<sup>[28]</sup> we demonstrated a first proof of concept of the soft pop-up arm while performing free body motion. In this paper, we propose a redesigned version of the arm where the yaw and pitch DOF are modified to allow for a larger range of motion and match the required workspace for ESD procedures,<sup>[27]</sup> and to avoid occluding visualization of the surgical area. Furthermore, we fabricated the soft pop-up arm entirely with biocompatible materials: MED-6033 and

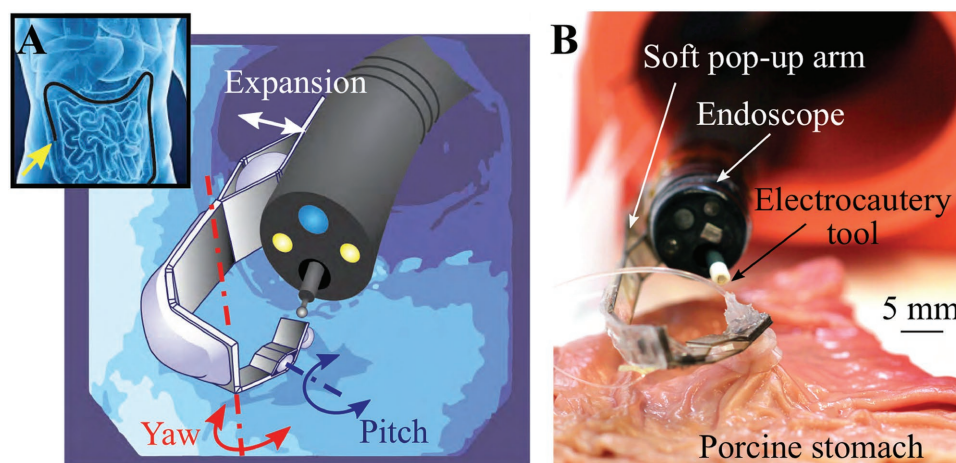


**Figure 7.** Multiarticulated soft pop-up robotic arm. A) Concept of the system: endoscope navigating in the GI tract and detail of the arm mounted at the tip of the endoscope. B) Soft pop-up arm performing tissue countertraction during an ex vivo test on a porcine stomach.

MED4-4220 were used for the SFMA, 3M 9877 as adhesive, and as structural and flexible materials, optically clear polyester sheets (0.254 and 0.025 mm thick, respectively) were used (Dura-Lar Film, Grafix, USA) to avoid occluding the endoscope camera's field of view as much as possible. An end-effector consisting of a soft suction-based gripper (described in ref. [35]) is fixed at the tip of the robotic arm. Currently, the vacuum line of the gripper is not integrated in the arm laminate. Here, the functionality of proposed system was tested for the first time ex vivo on a porcine stomach (Figure 7B), to evaluate the possibility of performing tissue countertraction (Figure S4 and Movie S3, Supporting Information). Successful endoluminal tissue manipulation was performed. Furthermore, successful integration of the soft pop-up arm on the endoscope was demonstrated: the arm does not hamper the endoscope movement during operation.

### 3. Discussion

We have introduced a hybrid manufacturing paradigm which combines pop-up book MEMS fabrication technology with techniques from soft lithography to build smart millimeter-scale actuators with user-defined distributed compliance. Our method is low cost and enables batch manufacturing. The benefits of our approach include monolithic integration of actuation (i.e., fluidic lines and microactuators) and sensing elements (i.e., conductive traces for capacitive sensing) along with other mechanical components, preserving the accuracy in the fabrication process and obviating the need for manual intervention to assemble discrete parts, thus allowing scalability and nearly arbitrary design complexity. We exploit soft fluidic actuation, thus avoiding the need for high voltages or temperatures and guaranteeing a safe interaction with biological tissue. Our method allows flexibility in material selection—we have specifically chosen to use biocompatible materials, paving the way to design and develop smaller, smarter, softer robots for biomedical applications. The introduction of rigid structures provides the necessary stiffness to the mechanisms in order to improve their performance in terms of force output and motion

reliability without compromising a safe interaction with biological tissue.

Biocompatible soft materials that can be treated with oxygen plasma have been selected to allow integration of soft components with pop-up book MEMS by exploiting chemical surface functionalization. Furthermore, a biocompatible adhesive has been selected. We have extensively characterized the reliability of the biocompatible materials and the fabrication method: (1) by running chemical surface characterizations to ensure the success of the surface modifications involved in the process; and (2) by testing the peel strength to ensure the mechanical reliability of the bonding between the SFMA and the rigid pop-up structures, as well as between the adhesive and different material substrates.

We demonstrated two different classes of soft fluidic microactuators and two different design strategies of integration into pop-up structures (to build hybrid soft pop-up actuators). We illustrate the possibility of scaling our technology by fabricating prototypes at different scales ranging from 5 to 1.25 mm. We also investigated the possibility of integrating sensing capabilities to achieve proprioceptive actuation and scaling this at all the above mentioned dimensions. Each actuator was characterized running different tests, namely, life cycles, blocked torque, maximum deflection, stiffness, and maximum speed. The soft pop-up actuators show greater predictability in their trajectory during motion with respect to their fully soft counterparts. The current maximum speed of the actuators is limited by the maximum speed that the experimental setup can achieve and will be improved in future work by embedding on-board valving. A summary of the different actuator characteristics is reported in Table 1 and Table S6 (Supporting Information), along with performance indices such as maximum work output, maximum power output, and maximum power density. Power density is indicated normalized with respect to the volume as well as to the mass of the actuator. In general, we can observe an increase in the performance of the actuators in terms of work and power output when we introduce the pop-up structure. Despite the increase in mass and volume of the actuators (due to the introduction of the rigid structure) the power density of the soft

**Table 1.** Summary of actuators characteristics.

Actuator type	Scale [mm]	Blocked torque [mN m]	Maximum deflect. [°]	Max speed [° s <sup>-1</sup> ]	Max work output [J]	Max power output [W]	Max power density [W m <sup>-3</sup> ]	Max power density [W kg <sup>-1</sup> ]
BFS	5	0.55	170.1	15	$1.64 \times 10^{-3}$	$6.26 \times 10^{-3}$	$3.32 \times 10^4$	$5.45 \times 10^1$
	2.5	0.32	142.8	22.5	$0.79 \times 10^{-3}$	$2.02 \times 10^{-3}$	$2.10 \times 10^4$	$2.2 \times 10^1$
	1.25	0.27	142.3	120	$0.67 \times 10^{-3}$	$0.32 \times 10^{-3}$	$1.69 \times 10^4$	$7.81 \times 10^0$
IMJ	5	10.68	75.3	8.3	$1.40 \times 10^{-2}$	$9.69 \times 10^{-2}$	$4.51 \times 10^5$	$4.66 \times 10^2$
	2.5	3.34	72	12.6	$4.19 \times 10^{-3}$	$1.91 \times 10^{-2}$	$2.42 \times 10^5$	$2.10 \times 10^2$
	1.25	0.94	55.3	16.9	$0.91 \times 10^{-3}$	$3.08 \times 10^{-3}$	$8.51 \times 10^4$	$7.71 \times 10^1$
EMJ	5	3.6	60.9	8.7	$3.82 \times 10^{-3}$	$2.52 \times 10^{-2}$	$1.35 \times 10^5$	$1.00 \times 10^2$
	2.5	1.46	89.8	10	$2.29 \times 10^{-3}$	$1.31 \times 10^{-2}$	$1.37 \times 10^5$	$9.73 \times 10^1$
	1.25	0.8	91.5	18	$1.27 \times 10^{-3}$	$4.06 \times 10^{-3}$	$1.69 \times 10^5$	$7.67 \times 10^1$

pop-up actuators is almost one order of magnitude greater with respect to the fully soft counterparts. The rigid structure limits the compliance of the mechanisms to discrete locations, thus providing a more effective conversion of the input pressure and volume into output forces and motion, even if the target on which we are acting has similar or greater stiffness than the actuator. In the fully soft case, the stiffness mismatch between the target and the actuator can cause the latter to deform in the direction of less compliance, thus away from the target, resulting in a less effective transmission of the input pressure and volume into the desired motion and forces. We demonstrated the potential of soft pop-up fabricated mechanisms in surgical applications by building a multiarticulated robotic arm that is integrated on a flexible endoscope and performed a tissue countertraction experiment in an ex vivo test. The proposed device augments distal dexterity without disrupting the surgical workflow since it can be mounted externally onto conventional instrumentation, leaving the endoscope working channel free for passing additional tools (such as electrocautery tools, shown in Figure 7). Three fluidic actuation lines are necessary for the arm actuation and they can be integrated on an overtube running along the endoscope. Fluidic lines are commonly integrated in endoscopic platforms for cleaning the camera and inflating the GI tract during navigation. In addition, fluidic actuation is commonly used to inflate navigation aids, for instance in double balloon endoscopy.<sup>[36]</sup> The primary aim of the proposed robotic arm is to serve as a demonstrator of the soft pop-up technology. This is the first ex vivo demonstration of combining hard and soft complex biocompatible materials with a low cost, monolithic fabrication technique, which enables millimeter-scale mechanisms with integrated sensing and actuation with the intent of creating novel surgical end-effectors. In the future, more work will be done in order to make this system suitable for an animal (in vivo) experiment. In particular, we will integrate the arm in a soft sleeve that the surgeon can pull (from outside the body) to free the mechanism in a safe and quick manner: we will explore currently available technologies for a reliable integration of the arm and the actuation lines on the endoscope, similarly to what is currently done for endoscopic overtubes in double balloon endoscopy. Furthermore, we will improve the current prototype focusing on designing the whole structure of the arm to be foldable and

deployable at the surgical site, in order to minimize the impact on endoscope navigation in the GI tract.

#### 4. Experimental Section

SFMA are manufactured using soft lithography (Figure 2A–H). Two silicon wafers were prepared: one patterned (height of features is 80 μm) with SU-8 photoresist (MicroChem Corp., MA, USA) and one blank. Both wafers were placed in an evacuated chamber with an open vessel containing a few drops of trichloro(1H,1H,2H,2H-perfluorooctyl)silane (Sigma-Aldrich) for at least 3 h. MED-6033 and MED4-4220 were poured respectively onto a blank and a patterned wafer, and degassed for 5 min in a vacuum chamber at -100 kPa. Subsequently, the wafers were rotated at different speeds. For the 5 mm scale actuators, MED-6033 was spin-coated at 270 rpm resulting in a 0.42 mm thick layer and MED4-4220 was spin-coated at 350 rpm resulting in a 0.38 mm thick layer (thus the membrane thickness is 0.3 mm). For the 2.5 mm scale actuators, MED-6033 was spin-coated at 310 rpm resulting in a 0.36 mm thick layer and MED4-4220 was spin-coated at 380 rpm resulting in a 0.3 mm thick layer (thus the membrane thickness was 0.22 mm). For the 1.25 mm scale actuators, MED-6033 was spin-coated at 350 rpm resulting in a 0.3 mm thick layer and MED4-4220 was spin-coated at 420 rpm resulting in a 0.23 mm thick layer (thus the membrane thickness was 0.15 mm). For each case, the spin time was 100 s. MED-6033 and MED4-4220 were cured at 150 and 65 °C, respectively, for 30 min. Subsequently, the layers were peeled off from the wafers using a flexible support made with a 25 μm polyimide film on top of a Gel-Pak 8 film (a flexible substrate material with a tacky surface to hold the layers during processing and/or assembly). Alignment holes as well as additional features such as release cuts were laser machined (the soft layer was aligned with the laser system exploiting three fiducial markers that were embossed on the wafer mold). At this point, the blank layer was bonded together with the patterned layer using O<sub>2</sub> plasma (65 W for 30 s) treatment (alignment holes were cut through, removed from each sample, and used to realign the layers during bonding). After bonding, the soft parts that had been cut (release cut) were peeled off, leaving the SFMA on the flexible support (Figure 3A,E). Hard layers were machined separately at the laser (Figure 2I), cleaned with isopropyl alcohol and dried. The hard layer that needs to be bonded to the soft layer was treated with a 65 W O<sub>2</sub> plasma for 60 s and immediately placed in an aqueous solution of 5% v/v (APTES 99% for 20 min (Figure 2J,K). The layer was then washed with DI water and let dry. Afterward, the soft layer was exposed to O<sub>2</sub> plasma and put in conformal contact with the amine-functionalized surface for a few minutes using alignment pins to ensure correct realignment (Figure 2L,M). At this point, the soft/hard layer was laminated together with the remaining necessary layers and they were bonded together using the 3M 9877 adhesive under pressure

(Figure 2N,O). Subsequently, a last step of machining was performed in order to release the mechanisms from the laminate scaffold (Figure 2P,Q). At this point, tubes with internal diameter of 0.254 mm (Micro Renathane Catheter Tubing, Braintree Scientific, USA) were inserted (through the pipe insertion point shown in Figure 1B,F) and the mechanisms were pressurized with water to provide actuation.

## Supporting Information

Supporting Information is available from the Wiley Online Library or from the author.

## Acknowledgements

The authors gratefully acknowledge support from DARPA (Award # FA8650-15-C-7548) and the Wyss Institute for Biologically Inspired Engineering.

## Conflict of Interest

The authors declare no conflict of interest.

## Keywords

actuators, advanced manufacturing, sensors, soft robotics, surgical robotics

Received: May 20, 2017

Revised: June 22, 2017

Published online:

- [1] B. P. M. Yeung, T. Gourlay, *Int. J. Surg.* **2012**, *10*, 345.
- [2] L. L. Swanstrom, *Gastroenterology* **2011**, *140*, 1150.
- [3] A. Loeve, P. Breedveld, J. Dankelman, *IEEE Pulse* **2010**, *1*, 26.
- [4] H. Aihara, N. Kumar, M. Ryou, W. Abidi, M. B. Ryan, C. C. Thompson, *Gastrointest. Endosc.* **2014**, *80*, 495.
- [5] H. Yamamoto, *Nat. Rev. Gastroenterol. Hepatol.* **2012**, *9*, 519.
- [6] V. Vitiello, S.-L. Lee, T. P. Cundy, G.-Z. Yang, *IEEE Rev. Biomed. Eng.* **2013**, *6*, 111.
- [7] D. Rus, M. T. Tolley, *Nature* **2015**, *521*, 467.
- [8] L. Wang, F. Iida, *IEEE Rob. Autom. Mag.* **2015**, *22*, 3.
- [9] M. Cianchetti, M. Calisti, L. Margheri, M. Kuba, C. Laschi, *Bioinspiration Biomimetics* **2015**, *10*, 35003.
- [10] K. Suzumori, S. Endo, T. Kanda, N. Kato, H. Suzuki, *Proc. of IEEE Int. Conf. on Robotics and Automation*, IEEE, Roma, Italy **2007**, pp. 4975–4980.
- [11] A. D. Marchese, C. D. Onal, D. Rus, *Soft Rob.* **2014**, *1*, 75.
- [12] B. Mazzolai, V. Mattoli, L. Beccai, **2017**, *Advances in Unconventional Computing*, *23*, 687.
- [13] P. Polygerinos, Z. Wang, K. C. Galloway, R. J. Wood, C. J. Walsh, *Rob. Auton. Syst.* **2015**, *73*, 135.
- [14] E. T. Roche, R. Wohlfarth, J. T. B. Overvelde, N. V. Vasilyev, F. A. Pigula, D. J. Mooney, K. Bertoldi, C. J. Walsh, *Adv. Mater.* **2014**, *26*, 1200.
- [15] M. Manti, V. Cacucciolo, M. Cianchetti, *IEEE Rob. Autom. Mag.* **2016**, *23*, 93.
- [16] T. Ranzani, G. Gerboni, M. Cianchetti, A. Menciassi, *Bioinspiration Biomimetics* **2015**, *10*, 035008.
- [17] M. Cianchetti, T. Ranzani, G. Gerboni, T. Nanayakkara, K. Althoefer, P. Dasgupta, A. Menciassi, *Soft Rob.* **2014**, *1*, 122.
- [18] C. Bergeles, G.-Z. Yang, *IEEE Trans. Biomed. Eng.* **2014**, *61*, 1565.
- [19] K. Suzumori, S. Iikura, H. Tanaka, T. Corporation, K. Suzumori, S. Iikura, H. Tanaka, *Proc. of IEEE on Micro Electro Mechanical Systems (MEMS): An Investigation of Micro Structures, Sensors, Actuators, Machines and Robots*, IEEE, Nara, Japan **1991**, pp. 204–209.
- [20] J. Paek, I. Cho, J. Kim, *Sci. Rep.* **2015**, *5*, 10768.
- [21] S. Wakimoto, K. Ogura, K. Suzumori, Y. Nishioka, *Proc. of IEEE Int. Conf. on Robotics and Automation*, IEEE, Kobe, Japan **2009**, pp. 556–561.
- [22] Y. Watanabe, M. Maeda, N. Yaji, R. Nakamura, H. Iseki, *IEEE 20th Int. Conf. on Micro Electro Mechanical Systems (MEMS)*, IEEE, Hyogo, Japan **2007**, pp. 659–662.
- [23] H. Okayasu, J. Okamoto, M. Fujie, H. Iseki, *Proc. of the 2005 IEEE Int. Conf. on Robotics and Automation*, IEEE, Barcelona, Spain **2005**, pp. 2890–2896.
- [24] J. P. Whitney, P. S. Sreetharan, K. Y. Ma, R. J. Wood, *J. Micromech. Microeng.* **2011**, *21*, 115021.
- [25] P. S. Sreetharan, J. P. Whitney, M. D. Strauss, R. J. Wood, *J. Micromech. Microeng.* **2012**, *22*, 055027.
- [26] J. B. Gafford, R. J. Wood, C. J. Walsh, *IEEE Sens. J.* **2016**, *16*, 69.
- [27] J. B. Gafford, T. Ranzani, S. Russo, H. Aihara, C. Thompson, R. J. Wood, C. J. Walsh, *IEEE Int. Conf. on Robotics and Automation (ICRA)*, IEEE, Stockholm, Sweden **2016**, pp. 4398–4405.
- [28] S. Russo, T. Ranzani, J. B. Gafford, C. J. Walsh, R. J. Wood, *IEEE Int. Conf. on Robotics and Automation (ICRA)*, IEEE, Stockholm, Sweden **2016**, pp. 750–757.
- [29] J. Gafford, T. Ranzani, S. Russo, A. Degirmenci, S. Kesner, R. Howe, R. Wood, C. Walsh, *J. Med. Devices* **2017**, *11*, 011007.
- [30] S. Varadarajulu, S. Banerjee, B. A. Barth, D. J. Desilets, V. Kaul, S. R. Kethu, M. C. Pedrosa, P. R. Pfau, J. L. Tokar, A. Wang, L.-M. Wong Kee Song, S. A. Rodriguez, *Gastrointest. Endosc.* **2011**, *74*, 1.
- [31] <https://nusil.com/services/downloadfile.ashx?productcode=MED4-4220&originalname=MED4-4220.pdf>, July **2017**, NuSil biocompatible silicone elastomer MED4-4220 datasheet.
- [32] <https://nusil.com/services/downloadfile.ashx?productcode=MED-6033&originalname=MED-6033P.pdf>, July **2017**, NuSil biocompatible silicone elastomer MED-6033 datasheet.
- [33] <http://multimedia.3m.com/mws/media/791992O/med-spec-tape-clinical-summary.pdf>, July **2017**, 3M-9877 Biocompatible adhesive datasheet.
- [34] V. Sunkara, D.-K. Park, Y.-K. Cho, *RSC Adv.* **2012**, *2*, 9066.
- [35] T. Ranzani, S. Russo, C. J. Walsh, R. J. Wood, *The Hamlyn Symp. on Medical Robotics*, Imperial College London and the Royal Geographical Society, London, UK **2016**.
- [36] H. Yamamoto, C. Ell, H. Kita, A. May, *Video Capsule Endoscopy*, Springer, Berlin **2014**, pp. 113–118.